Noncanonical hedgehog pathway activation through SRF–MKL1 promotes drug resistance in basal cell carcinomas

Ramon J Whitson[1,2], Alex Lee[3], Nicole M Urman[2], Amar Mirza[1,2], Catherine Y Yao[1,2], Alexander S Brown[1,2], Jiang R Li[1,2], Gautam Shankar[1,2], Micah A Fry[3], Scott X Atwood[1,2,4], Eunice Y Lee[2], S Tyler Hollmig[2], Sumaira Z Aasi[2], Kavita Y Sarin[1,2], Matthew P Scott[2], Ervin H Epstein Jr[3], Jean Y Tang[1,2] & Anthony E Oro[1,2]

Hedgehog pathway–dependent cancers can escape Smoothened (SMO) inhibition through mutations in genes encoding canonical hedgehog pathway components; however, around 50% of drug-resistant basal cell carcinomas (BCCs) lack additional variants of these genes. Here we use multidimensional genomics analysis of human and mouse drug-resistant BCCs to identify a noncanonical hedgehog activation pathway driven by the transcription factor serum response factor (SRF). Active SRF along with its coactivator megakaryoblastic leukemia 1 (MKL1) binds DNA near hedgehog target genes and forms a previously unknown protein complex with the hedgehog transcription factor glioma-associated oncogene family zinc finger-1 (GLI1), causing amplification of GLI1 transcriptional activity. We show that cytoskeletal activation through Rho and the formin family member Diaphanous (mDia) is required for SRF–MKL-driven GLI1 activation and for tumor cell viability. Remarkably, nuclear MKL1 staining served as a biomarker in tumors from mice and human subjects to predict tumor responsiveness to MKL inhibitors, highlighting the therapeutic potential of targeting this pathway. Thus, our study illuminates, for the first time, cytoskeletal-activation-driven transcription as a personalized therapeutic target for combatting drug-resistant malignancies.

Targeted inhibition of pathways with a causative oncogenic role in drug-naive tumors provides a selective environment for outgrowth of drug-resistant clones[1]. Mutations that hinder drug binding at the intended target, promote drug efflux, or enhance activation of alternative signaling pathways are major factors that affect tumor fitness[2–5]. Defining the role of growth cues within the tumor microenvironment remains a growing area of investigation[6–8].

BCC of skin is the most common human cancer and provides an ideal system for study of tumor evolution. BCCs invariably result from mutations in the genes encoding the hedgehog receptors Patched (*PTCH1*) or Smoothened (*SMO*), causing constitutive hedgehog pathway activation. Vismodegib, an agent targeted to SMO, recently received Food and Drug Administration approval as a treatment for advanced BCCs. Unfortunately, fewer than 50% of patients with advanced or metastatic BCCs respond to vismodegib at the time of treatment, with an additional 20% acquiring secondary resistance during the first year of treatment[9–11]. Similar to sporadic drug-naive BCCs, drug-resistant clones in patients uniformly maintain activation of hedgehog target genes[12], highlighting an undiminished dependence on the hedgehog pathway for growth of drug-resistant tumors.

Mutations in genes related to the canonical hedgehog pathway that cause maintenance of GLI1 transcription factor activity in vismodegib-resistant BCCs have recently been uncovered in or downstream of *SMO*. These include mutations generating constitutively active SMO, loss of the gene encoding hedgehog inhibitor suppressor of fused (*SUFU*), amplification of *GLI2* and *CCND1*, and activation of the polarity kinase *aPKC*[12–14]. Yet, through our previous sequencing efforts, we found that approximately 50% of human treatment-resistant BCCs contained no additional hedgehog pathway variants, and the majority of *SMO* variants identified were nonfunctional despite tumors maintaining elevated hedgehog activation[12,15]. These data strongly support the existence of one or more unidentified pathways merging downstream of the hedgehog pathway to stimulate noncanonical activation of GLI1 to promote drug resistance.

Here we carry out multidimensional genomics analysis using a new mouse model for BCC resistance and human-derived tumors to identify a key role for the transcription factor (TF) SRF in the evolution of drug resistance. SRF was previously reported to drive two mutually exclusive gene regulation programs through association with transcriptional cofactors ELK1 or MKL1 and MKL2 (MKL1/2, also known as MRTF-A/B and MAL)[16–20]. In the latter pathway, RhoA activates the actin-polymerizing proteins Rho-associated protein kinase (ROCK) and mDia, causing restructuring of globular actin to filamentous actin (G- and F-actin, respectively). This restructuring liberates cytoplasmic MKL1, allowing this TF to move into the nucleus to activate MKL-dependent gene expression. We define the

SRF–MKL1 cytoskeletal signaling pathway as a nonclassical component of the hedgehog pathway that amplifies downstream GLI1 activation and drug-resistant tumor growth. Additionally, we show that MKL1 inhibitors have considerable efficacy in treating drug-resistant BCCs *in vivo*, implicating the cytoskeletal-sensing SRF–MKL1 pathway as a promising new therapeutic target for resistant BCCs.

RESULTS

BCCs in PTC53 mice mimic phenotypes of resistant BCCs in humans

Previous mutational landscape analysis of human-derived drug-resistant BCCs uncovered variants in genes encoding components of the canonical hedgehog pathway[12,13]; however, less than half of these tumors contained canonical mutations, many of which were nonfunctional[15]. This revealed the existence of one or more unknown yet prevalent noncanonical pathways promoting drug-resistant tumor growth in BCCs. To identify and characterize these noncanonical pathways, we investigated a new mouse model for tumor drug resistance that closely resembles the clinical attributes of human BCCs. We used *Ptch1*^{+/−}; KRT14-Cre-ER; *Trp53*^{fl/fl} (PTC53-BCC) mice, which were previously reported to develop primary tumors resembling human BCCs after a single dose of radiation[21]. Drug-naive tumors were passaged into NOD-SCID recipient mice, which were intermittently treated with the SMO inhibitor GDC-619 over several cycles spanning a 3-month period (**Fig. 1a,b** and **Supplementary Fig. 1a,f**). Remarkably, intermittent SMO inhibition resulted in generation of both sensitive and resistant BCCs (sBCCs and rBCCs, respectively)

that resembled human BCCs in histology and marker expression (**Fig. 1c–g**). SBCCs and rBCCs were defined as tumors with a net regression and active growth, respectively, in the presence of the SMO inhibitor (**Supplementary Fig. 1b**). Like human BCCs, nodular, morpheic, and Pinkus subtypes were represented, providing evidence that these histological subtypes do not correlate with resistance to SMO inhibitors (**Fig. 1c** and data not shown).

To further characterize our mouse tumors, we identified expression changes using whole-transcriptome analysis through RNA sequencing (RNA-seq). Differential expression analysis uncovered significantly up- or downregulated mRNAs in rBCCs relative to sBCCs (**Fig. 1d**). Similar to human rBCCs, mouse rBCCs expressed high levels of *Gli1* and *Ptch1* at both the mRNA and protein level (**Fig. 1e–g**), indicating hedgehog pathway activation. These tumors lacked markers for other keratinocyte-derived tumors, such as immunoreactivity to the MAP kinase pathway marker phosphorylated ERK (**Supplementary Fig. 1c,d**). Additional BCC markers (EPCAM, BCL2, GLI2, and ACTA2) were expressed at high levels relative to the squamous cell carcinoma markers involucrin (IVL), SOX2, and CDKN2A (**Supplementary Fig. 1e**). Thus, we conclude that the PTC53-BCC mouse line is a new source of clinically relevant rBCCs.

Multidimensional genomics uncovers activated SRF in human and mouse rBCCs

To shed light on the mechanisms underlying drug resistance that maintain elevated hedgehog signaling, we reasoned that additional TFs provide compensatory growth signaling to promote noncanonical
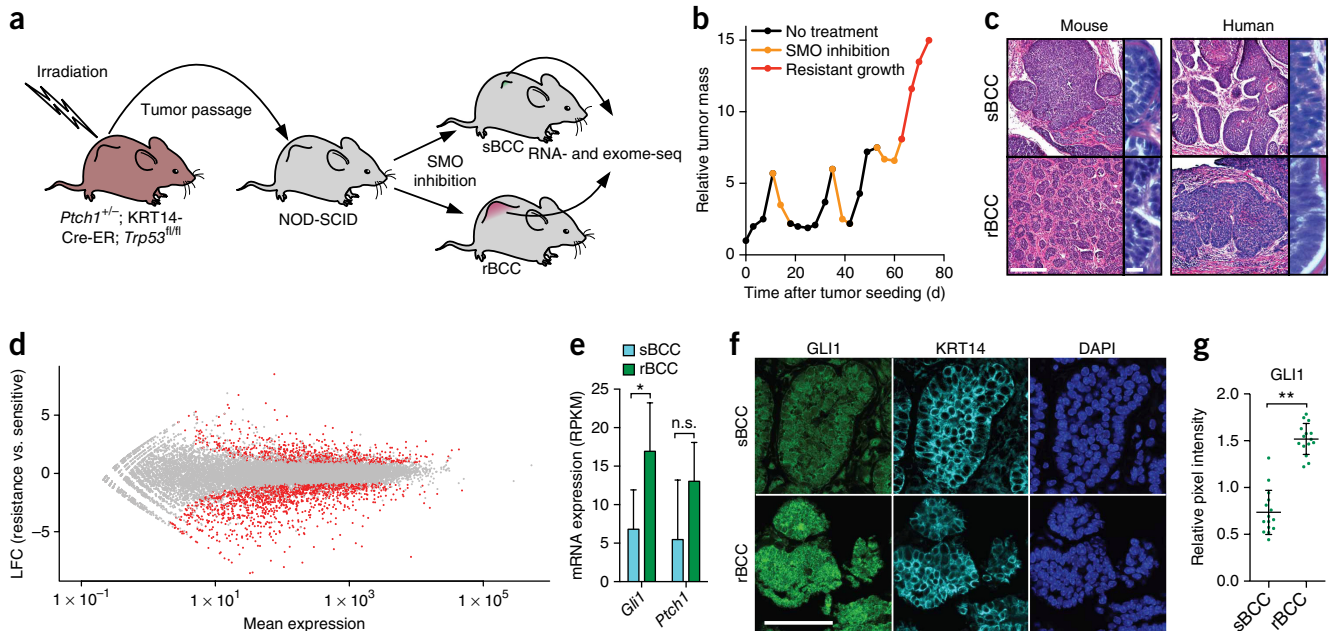

Figure 1 The PTC53 BCC mouse model produces SMO-inhibitor-resistant tumors with human tumor characteristics. (**a**) Schematic of rBCC tumor generation using PTC53 mice. Exome-seq, whole-exome sequencing. (**b**) Representative growth curve (from the 16 resistant tumors used in our study) illustrating resistant tumor formation after three cycles of SMO inhibitor treatment. (**c**) Representative H&E stain of sBCCs and rBCCs from mice and humans showing similar histology. For mice, $n = 16$ rBCCs and 14 sBCCs; for humans, $n = 24$ rBCCs and 11 sBCCs. Scale bars, 100 μm in low-magnification fields (left) and 10 μm in high-magnification fields (right). (**d**) Genome-wide differential transcript expression sequencing (DE–seq) plot highlighting genes with significantly changed expression in resistant versus sensitive mouse tumors. Transcripts with expression $\geq \pm \log_2$ (fold change) (LFC) and $P \leq 0.05$ are highlighted in red. P was determined using the DESeq negative binomial distribution model. (**e**) *Gli1* and *Pcth1* mRNA expression obtained from RNA-seq data in **d** for mouse sBCCs and rBCCs. Data represent means from four tumors per condition + s.e.m. in **e**; $n = 4$ sBCCs and 4 rBCCs in **d** and **e**. RPKM, reads per kilobase of transcript per million mapped reads. (**f**) Left, GLI1 protein expression indicated by immunofluorescence (IF) staining in mouse sBCCs and rBCCs. Middle, cytokeratin-14 (KRT14) stain demarcating epithelial-derived BCCs in tissue sections. DAPI demarcates all nuclei in each field. Scale bar, 100 μm. (**g**) Quantification of GLI1 protein expression in **f** using pixel intensity measurements ($n = 15$ fields measured for each condition). Data represent means ± s.e.m. A Student's *t*-test was used to determine the differential expression significance in **e** and **g**. *$P < 0.05$, **$P < 0.001$; n.s., not significant.
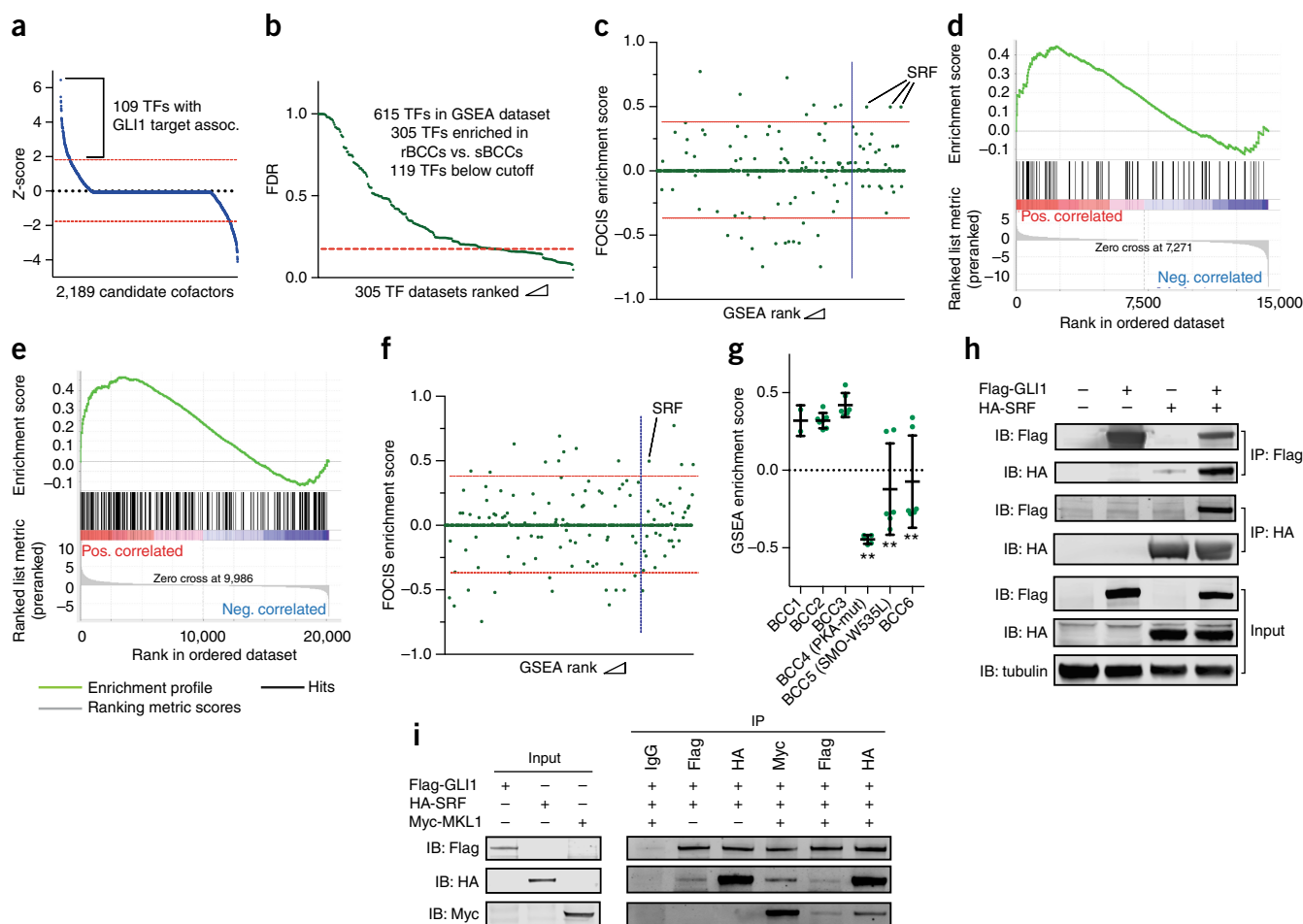
Figure 2 Multicomponent genomic analyses identifies SRF as a previously unrecognized hedgehog cofactor with aberrant activation in rBCCs. (**a**) Enrichment of putative GLI1 transcriptional coactivators determined using the FOCIS algorithm. The red lines indicate the cutoff for the top and bottom 5% of positively and negatively enriched cofactors, respectively. (**b**) Results from GSEA carried out using the TRANSFAC database for TF targets identifying TFs with increased activity in rBCCs versus sBCCs. The red line indicates the cutoff where the false discovery rate (FDR) reaches 0.2 with $P < 0.05$; a Kolmogorov–Smirnov test was used to determine statistical significance for GSEA hits. (**c**) Results from a multicomponent analysis combining the FOCIS and GSEA data sets shown in **a** and **b**, respectively, showing enrichment of SRF in both data sets. The red lines indicate the cutoff for the top and bottom 5% of FOCIS hits, and the blue line indicates the cutoff for the top 10% of enriched targets in GSEA. (**d,e**) Representative plots of GSEA enrichment data showing increased activity in mouse (**d**) and human (**e**) rBCCs. (**f**) Results from a multicomponent analysis using RNA-seq data from human BCCs showing SRF enrichment in resistant tumors. The red and blue lines are as described in **c**. (**g**) Results from GSEA in individual human rBCCs showing SRF enrichment only in tumors without activating mutations in genes encoding canonical hedgehog pathway activators. An unpaired Student's *t*-test was used to compare the average of BCC1–BCC3 and BCC4–BCC6 individually. **$P < 0.001$ for SRF GSEA enrichment of the indicated sample using all available TRANSFAC data sets. Data represent individual SRF data sets as means ± s.e.m. (**h**) Reciprocal co-IP blots in 293T cells using antibodies against Flag-GLI1 and HA-SRF. (**i**) Inverse co-IP blots in rabbit reticulocyte extracts using antibodies against Flag-GLI1, HA-SRF, and Myc-MKL1.

activation of GLI TFs downstream of SMO. Using the recently developed feature overlapper for chromosomal interval subsets (FOCIS) algorithm[22], we screened for TFs co-occupying sites near GLI1 to uncover its potential cofactors. This method compares input genomic coordinate data to a large data set of genomic binding information compiled from numerous data sets. Our input data set consisted of Flag-tagged GLI1 (Flag-GLI1) genomic binding data from a model of hedgehog-dependent medulloblastoma; this was the only tumor-derived GLI chromatin immunoprecipitation and sequencing (ChIP–seq) data available at the time (Online Methods). Using FOCIS, we ranked TFs with chromosomal occupancy profiles showing enrichment at GLI1 target genes and found 109 TFs with overlapping binding signatures (**Fig. 2a**). Next, we used our RNA-seq data to identify TFs with enhanced activation in rBCCs using the gene set enrichment

analysis (GSEA) TRANSFAC database. GSEA revealed 305 target gene expression profiles showing enrichment in resistant tumors as compared to sensitive tumors and highlighted selective activation of genes encoding a subset of TFs (**Fig. 2b**). To define TFs in this subset as putative GLI1 cofactors with both enriched occupancy at hedgehog target genes and selective activation in rBCCs, we carried out a multicomponent analysis that ranked the TFs with high scores in both the GSEA and FOCIS enrichment analysis. Of the 615 possible TFs, our multicomponent analysis identified SRF as the top candidate as a putative GLI1 cofactor with increased transcriptional activity in rBCCs (**Fig. 2c,d**).

To determine a role for SRF in human BCCs, we examined SRF activation using our human BCC transcriptome data sets[12]. GSEA revealed similar SRF enrichment in both mouse and human rBCCs (**Fig. 2d,e**),

and multicomponent analysis also revealed elevated SRF enrichment at GLI1 targets in human rBCCs (**Fig. 2f**). We divided individual subject samples into those with mutations in genes known to activate the canonical hedgehog pathway to confer resistance conferring resistance and those without such canonical variants. In samples with a high allele frequency for mutations in genes related to the classical hedgehog pathway, no SRF target gene enrichment was observed. However, in three of four tumors without a detectable canonical mutation, we observed positive enrichment for SRF target genes (**Fig. 2g**), suggesting that SRF activation is the predominant alternative pathway driving BCC resistance in tumors without *SMO* mutations. In accordance with this observation, SRF target gene enrichment arose in resistant mouse tumors exhibiting negligible changes in single-nucleotide variant (SNV) rate (**Supplementary Fig. 2a**). Previous studies indicated that 50% of SMO-inhibitor-resistant tumors lack *SMO* mutations in human subjects[9,12,15]. Similar to this subset of human resistant tumors, PTC53 mouse–derived rBCCs contained low frequencies of *Smo* variants (**Supplementary Fig. 2b**). Intriguingly, additional FOCIS analysis revealed SRF enrichment at GLI1 target sites using ChIP–seq data from medulloblastoma (**Fig. 2a–c**) but not at GLI1 occupancy sites in the developing central nervous system or at GLI3 sites during limb bud formation (**Supplementary Fig. 2c**), indicating that SRF binds to GLI sites in tumorigenic, but not developing, tissues. Pathway enrichment terms from human and mouse RNA-seq data comparing transcriptome signatures for rBCCs versus sBCCs (**Supplementary Fig. 2d,e**) suggest activation of cytoskeletal signaling networks[23]. Thus, we conclude that increased SRF transcriptional activity at GLI target genes correlates specifically with tumor resistance.

SRF and MKL1 are required for rBCC growth and elevated hedgehog pathway activity

Our bioinformatic analyses suggest that SRF functions to induce GLI1 activity through proximal binding to DNA (**Fig. 2a**). To determine whether GLI1 forms a complex with SRF, we carried out inverse coimmunoprecipitation (co-IP) experiments using Flag-GLI1 and hemagglutinin-tagged SRF (HA-SRF). Indeed, antibodies against Flag-GLI1 pulled down HA-SRF, and IP using HA resin pulled down HA-SRF and Flag-GLI1 in human embryonic kidney (HEK-293T) cells (**Fig. 2h**). Proximity ligation analysis (PLA) using two independent SRF antibodies highlighted a SRF–GLI complex *in situ* (**Supplementary Figs. 3** and **4**). We next investigated the role of SRF in rBCC growth. Knockdown of SRF expression caused a significant decrease in rBCC cell growth (**Fig. 3a** and **Supplementary Fig. 5c–e**) and downstream hedgehog pathway output, measured by a decrease in *Gli1* mRNA expression (**Fig. 3b**), in mouse cells resistant to the SMO inhibitor, vismodegib (**Supplementary Fig. 5a,b**). Taken together, our data indicate that SRF maintains downstream hedgehog activity and is necessary for rBCC growth.

SRF transduces a wide variety of environmental cues and is known to act downstream of p38 MAP kinase, MAP kinase kinase (MEK), protein kinase A (PKA), and MKL1 (refs. 24–27) to form distinct heterodimeric transcriptional complexes (**Fig. 3c**). To determine which upstream signals were required for SRF-driven BCC growth, we screened a panel of inhibitors in two distinct SMO-inhibitor-resistant mouse cell lines (ASZ001 and BSZ001) for those that could inhibit cell growth and *Gli1* expression; only the MKL inhibitor CCG-1423 was capable of this (**Fig. 3d–f** and **Supplementary Fig. 5i,l,r,s**), whereas inhibitors against other SRF-activating pathways (PKA, MEK–ERK, and p38) demonstrated little effect, even at doses well above their IC$_{50}$ (**Supplementary Fig. 5f–n**), supporting the specificity of MKL

inhibition. Direct knockdown of MKL1 or MKL2 expression and treatment with two structurally distinct MKL inhibitors, CCG-203971 and CCG-100602, produced similar results (**Supplementary Figs. 5t–v** and **6**). Human rBCCs reacted to MKL inhibition with a similarly potent response rate (**Fig. 3f** and **Supplementary Fig. 7**). To assess general toxicity, we measured the cell viability of nonmalignant epithelial cells treated with MKL inhibitors; we observed little response following treatment (**Supplementary Fig. 5o–q**), highlighting the tumor-specific nature of the signaling pathway. Finally, we used an inverse pulldown assay in rabbit reticulocyte lysates to test whether MKL1 formed a complex with GLI1 and SRF (**Fig. 2i**). We found that GLI1 and SRF were immunoprecipitated with Myc-tagged MKL1, supporting our conclusion that GLI1 forms a previously unknown complex with SRF and MKL1.

We next asked whether activation of MKL1 was sufficient to activate hedgehog target genes in nonmalignant cells. MKL1 is kept inactive in the cytoplasm through binding to monomeric G-actin via its N-terminal RPEL domain[28], and deletion of this domain results in nuclear accumulation of MKL1[20]. Expression of constitutively active MKL1 (MKL1-N*) in NIH-3T3 cells caused potentiation of hedgehog pathway activity following subthreshold SMO agonist (SAG) treatment, whereas full-length MKL1 (MKL1-FL) produced minimal activity following SAG treatment in wild-type cells (**Fig. 3g** and **Supplementary Fig. 5w**). These data suggest that upstream activation of MKL1 is required to potentiate expression of hedgehog target genes and highlight a requirement for low-level hedgehog activation. Thus, we conclude that MKL1 and SRF amplify the hedgehog pathway by potentiating *GLI1* expression.

GLI1–SRF occupies and regulates a distinct subset of target genes

To define the transcriptome-wide gene regulatory signature for MKL and SMO in rBCC cells, we carried out RNA-seq in mouse rBCC cells (ASZ001) treated with MKL and SMO inhibitors. RNA-seq analysis indicated that 1,448 genes were dependent on MKL and only 139 genes required SMO for expression, with 50 genes overlapping between these sets (**Fig. 3h,i**). To further investigate the mechanism underlying gene regulation by SRF and GLI1, we identified genomic regions directly occupied by these proteins using ChIP–seq in medulloblastoma cells. We identified 6,519 ChIP peaks for SRF and 4,638 peaks for GLI1, with 632 sites overlapping (**Fig. 3j**). Consistent with results from our FOCIS analyses (**Fig. 2a–c**), GLI1 occupied binding sites in close proximity to SRF ChIP peaks (**Fig. 3k,l**). ChIP peak profiles indicated SRF occupancy in the 5 untranslated region (UTR) of hedgehog pathway activators *GLI1* and *GLI2*, but not hedgehog repressors *GLI3* and *PTCH1* (**Fig. 3m** and **Supplementary Fig. 8a–c**), suggesting that SRF and MKL1 amplify hedgehog activity via regulating expression of hedgehog pathway activators.

Results from our multidimensional screen (**Fig. 2**) suggest that SRF binds to GLI1 target sites that are enriched in rBCCs, which led us to investigate whether SRF binding to hedgehog targets required MKL1 and/or GLI1. We performed SRF and MKL1 ChIP analyses followed by qPCR to determine state-dependent SRF–MKL1 occupancy at GLI1–SRF co-bound hedgehog target genes in mouse rBCC cells (ASZ001). Treatment with the MKL1 inhibitor CCG-1423 abolished the SRF–MKL1 ChIP signal at these sites (**Fig. 3n** and **Supplementary Fig. 9**), indicating that MKL1 activation is required for occupancy. Notably, GLI1 inhibition with the aPKC inhibitor PSI, previously shown to prevent GLI1 association with chromatin[14], abolished SRF–MKL1 occupancy at hedgehog target gene loci,

suggesting that GLI1 is also required for SRF–MKL1 recruitment to hedgehog target genes. In contrast, SRF binding sites with no associated GLI1 ChIP signal (for example, *FoxF1*) did not require MKL1 or GLI1 for SRF occupancy (**Fig. 3n**). We determined whether GLI1–SRF co-bound genes required MKL for expression using RNA-seq data from rBCC cells (**Fig. 3h,i**), and we found that *Gli1*, *Ccnd2*,

and *Actb*, but not *Gli2*, required MKL1 for expression (**Fig. 3o–r**), indicating that MKL1 promotes expression of a wide array of hedgehog target genes in rBCC cells. Taken together, our results suggest that GLI1 recruits SRF and MKL1 to hedgehog target gene loci and the SRF–MKL1 complex is required to maintain elevated expression of hedgehog target genes.
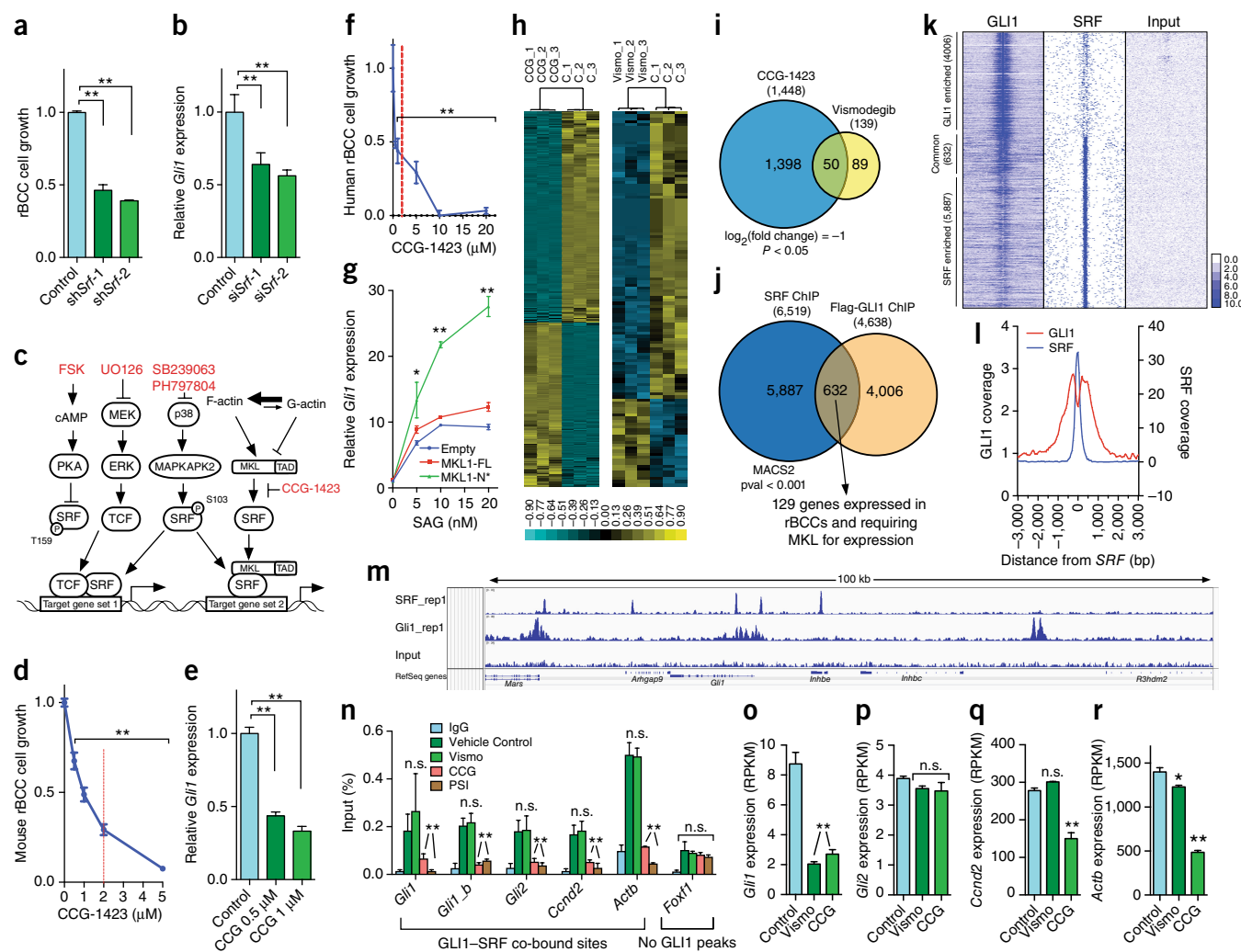
Figure 3 SRF and MKL1 are necessary for rBCC growth and potentiate hedgehog pathway activity. (**a**) Results from a MTS assay used to measure cell growth in ASZ001 cells with stable expression of antisense shRNAs against *Srf* and scrambled control shRNA; data show relative MTS absorbance at 490 nm for sh*Srf*-transfected cells compared to cells transfected with a scrambled control shRNA. $n = 3$ biological replicates (representing 3 separate wells per data point). (**b**) Results from qPCR of *Gli1* in ASZ001 cells with transient SRF knockdown. Cells were transfected with antisense siRNAs to transiently knock down expression of *Srf* or with scrambled control siRNA. $n = 3$ technical replicates per condition. (**c**) Schematic of the known SRF-activating pathways and associated inhibitors (shown in red). (**d**) Results from a MTS assay using the MKL inhibitor CCG-1423 in ASZ001 cells. Data points represent mean MTS absorbance ($n = 3$ biological triplicates as described in **a**) ± s.d. The red line indicates the previously reported IC_{50} for CCG-1423. (**e**) Relative expression of *Gli1* mRNA in mouse ASZ001 cells following CCG-1423 treatment. $n = 3$ technical replicates per condition. (**f**) Results from a MTS growth assay carried out in human rBCC cells (UW-BCC1) treated with the indicated concentration of MKL inhibitor. The red line indicates the previously reported IC_{50} for CCG-1423. $n = 3$ biological replicates (as described in **a**) per condition. (**g**) mRNA expression of *Gli1* in NIH-3T3 cells following SAG treatment in cells expressing MKL1-FL and MKL1-N*. $n = 3$ technical replicates per data point. (**h**) A heatmap of results from RNA-seq analysis used to determine differential expression of genes regulated by CCG-1423 (1 μM; left) and vismodegib (150 nM; right) in ASZ001 cells. (**i**) Graph showing the number of overlapped genes downregulated by CCG-1423 and vismodegib as determined through RNA-seq. (**j**) Graph showing SRF and GLI1 genome-wide binding profiles identified through ChIP–seq and overlap within respective genomic peak intervals. (**k**) ChIP–seq peak enrichment for GLI1- and SRF-bound loci across 6-kb genomic regions centered on SRF peaks. (**l**) Positional ChIP–seq peak enrichment for SRF relative to GLI1. (**m**) Representative snapshot of local ChIP–seq peak enrichment at the *Gli1* genomic locus. (**n**) ChIP followed by qPCR using oligonucleotides against the 5′ UTRs of *Gli1*, *Gli2*, *Ccnd2*, *Actb*, and *FoxF1*. Data represent mean qPCR fold enrichment over IgG control + s.d. (**o–r**) RPKM values from RNA-seq data for genes showing differential ChIP occupancy as determined in **n**. $n = 3$ biological replicates (described in **a**) per condition. Data in **a**, **b**, **e**, and **o–r** represent means for triplicate observations + s.e.m. Data in **f–g** represent means for triplicate observations ± s.e.m. A Student's *t*-test (two-tailed) was used to determine significance for pairwise observations. *$P < 0.05$, **$P < 0.001$. For all ChIP experiments, 150 nM, 1 μM, and 5 μM of vismodegib (vismo), CCG-1423 (CCG), and PSI, respectively, were administered.
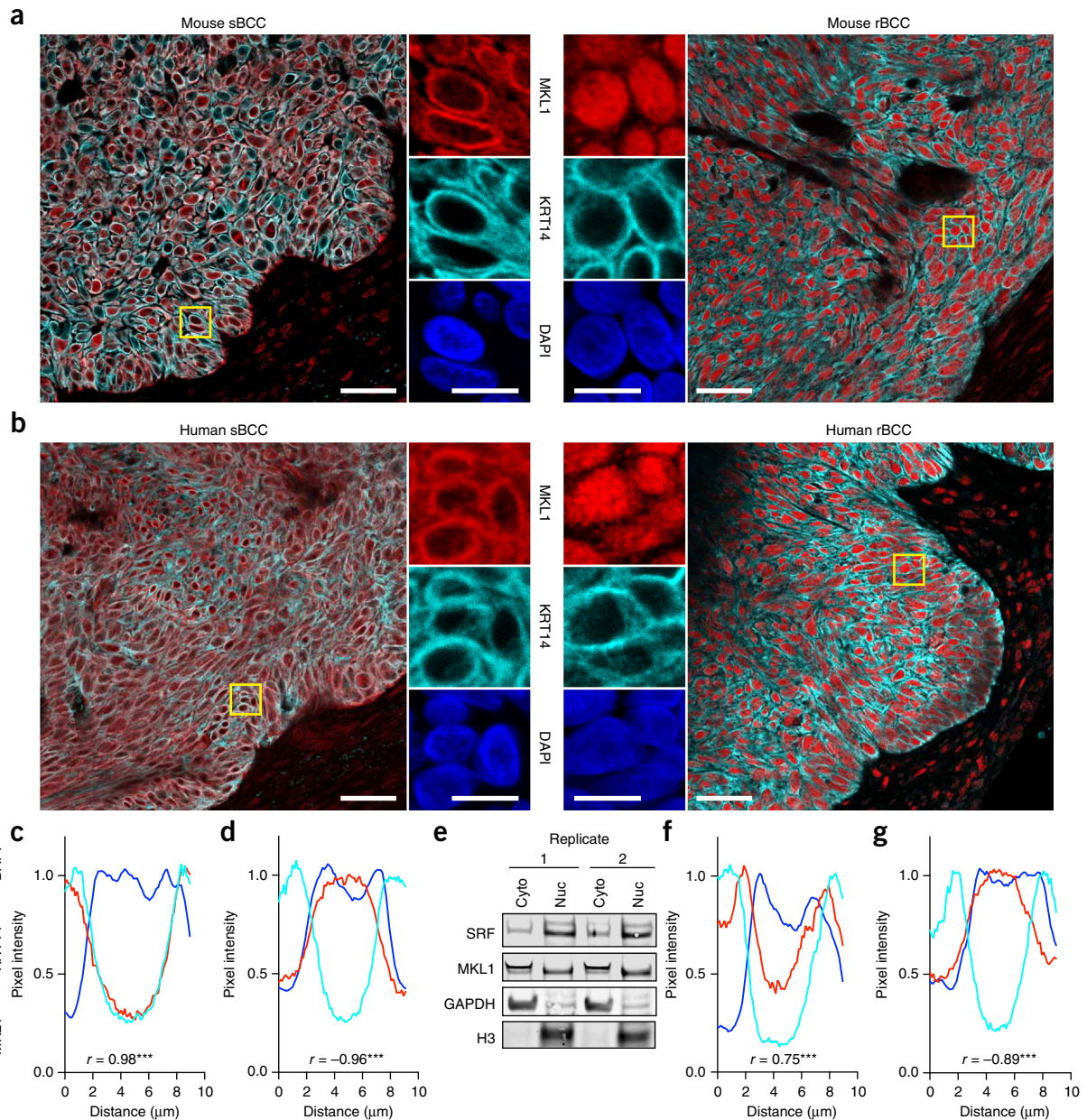
Figure 4 MKL1 accumulates in the nucleus in mouse and human rBCCs. (**a,b**) Representative immunofluorescence staining images from mouse (**a**) and human (**b**) BCC tumor sections following staining with antibodies against MKL1 and KRT14 (marker for cytoplasmic compartment); DAPI was used to mark nuclei. Scale bars, 50 μm and 10 μm in low- and high-magnification fields, respectively. In **a**, $n = 16$ rBCCs and 14 sBCCs; in **b**, $n = 24$ rBCCs and 11 sBCCs. (**c,d,f,g**) Compartmental quantification of tumor immunostaining shown in **a** and **b**. Pearson's coefficient was used to determine MKL1 staining correlation with KRT14 (cytoplasmic) staining. A two-tailed Student's t-test was used for statistical analysis. ***$P < 0.001$. (**e**) ASZ001 cellular fractionation followed by immunoblotting for SRF and MKL1 showing nuclear localization. Cyto, cytoplasmic; nuc, nuclear.

Nuclear MKL1 is present in the majority of rBCCs

Nuclear SRF–MKL1 activity requires elimination of G-actin-mediated inhibition of MKL1 in the cytoplasm[20,28]. Our bioinformatic analyses indicated that SRF–MKL1 was activated in rBCCs that had little change in SRF or MKL1 expression levels (**Supplementary Fig. 10**), leading us to investigate the nuclear accumulation of MKL1 in human and mouse BCC samples. Biochemical and immunohistological subcellular localization studies identified the presence of nuclear MKL1 in rBCCs, but not in sBCCs, in mice (**Fig. 4a,c,d**; $n = 16$ rBCCs and $n = 14$ sBCCs) and humans (**Fig. 4b,f,g**; $n = 24$ rBCCs and $n = 11$ sBCCs). Our human BCC data suggest that tumors with

constitutively active SMO (canonical resistance) do not require MKL1 activation for growth (**Fig. 2g**). To further explore this idea, we examined MKL1 compartmentalization in a mouse model of BCC resistance driven by the *SmoM2* mutation and, in accordance with our genomic data, found that MKL1 remains uniformly cytoplasmic when SMO is constitutively active (**Supplementary Fig. 11**). Subcellular fractionation using a rBCC mouse cell line (ASZ001) indicated that both SRF and MKL1 are abundant in the nucleus (**Fig. 4e**). Taken together, our data support a model in which SRF and MKL1 become activated in rBCCs via upstream signals promoting nuclear accumulation of MKL1.
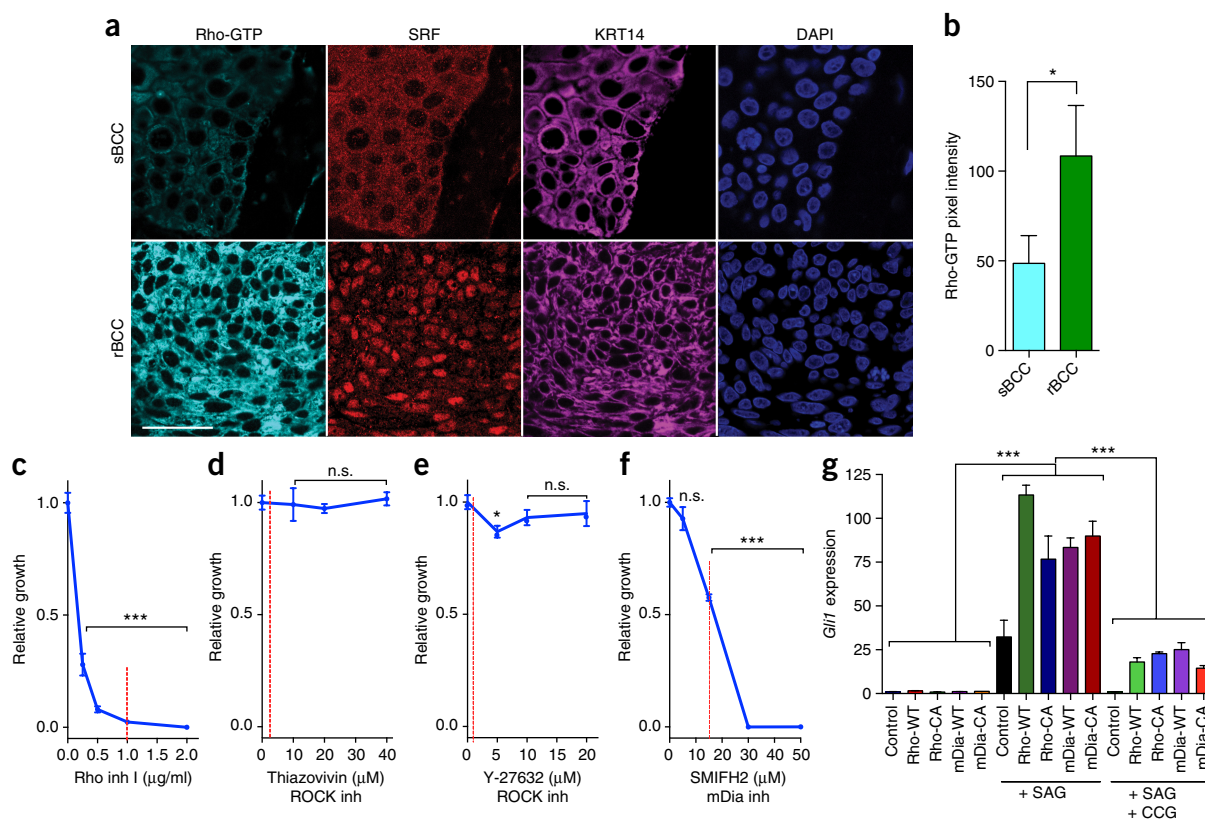
Figure 5 Downstream hedgehog activation requires active Rho and mDia. (**a**) Representative mouse tumor staining showing activated Rho (Rho-GTP), SRF, and KRT14 highlights tumor area; DAPI marks nuclei. $n = 6$ sBCCs and 6 rBCCs. Scale bar, 50 μm. (**b**) Quantification of Rho-GTP staining in **a**. Data show mean pixel intensity + s.d. A two-tailed Student's t-test comparing resistant versus sensitive was used for statistical analysis. $*P < 0.05$. (**c**–**f**) MTS growth assays in ASZ001 cells treated with inhibitors against Rho (Rho inhibitor I, **c**), Rho-associated protein kinase (thiazovivin, **d**; and Y-27632, **e**), and mDia (SMIFH2, **f**). The vertical red lines indicate the previously reported IC_{50} value for the indicated inhibitor. A two-tailed Student's t-test was used to calculate P for each data point compared to vehicle control (0) in **c**–**f**. Data in **c**–**f** represent means of $n = 3$ biological replicates (indicating 3 individual wells) ± s.e.m. for each data point compared to vehicle control (0). (**g**) $Gli1$ expression in NIH-3T3 cells expressing wild-type Rho (Rho-WT), constitutively active Rho (Rho-CA), wild-type mDia (mDia-WT), or constitutively active mDia (mDia-CA). Cells were treated with 20 nM SAG for 24 h after the indicated transfection and with 2 μM CCG-1423 (CCG) at the time of SAG treatment as indicated. Data represent mean qPCR induction of $Gli1$ expression using technical replicates ($n = 3$) + s.d. A Student's t-test was used in **c**–**g** to determine significance for indicated conditions versus control. $*P < 0.05$, $***P < 0.001$.

Actin cytoskeletal regulators are activated in resistant tumors and are required for BCC cell growth

Our observation that SRF–MKL1 nuclear localization potentiates GLI-driven BCC growth suggests that local tumor stimuli provide the necessary activation to drive resistance. Previous studies demonstrated that Rho activation is the primary driver of G-actin conversion to F-actin[29]. This conversion causes a local reduction in G-actin availability, resulting in decreased actin binding to the RPEL domain of MKL1. Release of G-actin binding causes MKL1 transport to the nucleus[30], which led us to examine the status of the Rho–actin pathway in rBCCs. Using a state-dependent antibody against activated Rho (Rho-GTP; **Supplementary Fig. 12**), we found that RhoA has increased activity in resistant tumors relative to sensitive tumors (**Fig. 5a**,**b** and **Supplementary Fig. 13**). rBCC cells displayed sensitivity to sub-IC_{50} concentrations of Rho inhibitor treatment (**Fig. 5c**), further implicating RhoA.

Active RhoA affects cytoskeletal changes by promoting actin polymerization through activation of ROCK and mDia[31,32]. We investigated the necessity of these individual Rho effectors in rBCC cells using specific inhibitors. ROCK inhibitors (thiazovivin and Y-27632) failed to suppress rBCC cell growth (**Fig. 5d**,**e**); however,

mDia inhibition (SMIFH2) potently blocked rBCC cell growth (**Fig. 5f**). To determine whether actin cytoskeletal mediators were sufficient to potentiate GLI1 activity, we expressed Rho and mDia in NIH-3T3 cells and observed increased phalloidin staining, indicating an increased concentration of F-actin (**Supplementary Fig. 14a**–**e**). We reasoned that F-actin accumulation would result in MKL1 activation, thereby causing hedgehog pathway activation. Indeed, elevated Rho and mDia expression promoted $GLI1$ expression following stimulation with SAG (**Fig. 5g**), suggesting that cytoskeletal activation is sufficient to potentiate the hedgehog pathway. This effect was abrogated by the MKL1 inhibitor CCG-1423, indicating that Rho and mDia act upstream of SRF–MKL1. Taken together, our data provide new mechanistic details for a link between cytoskeletal regulators and hedgehog pathway activation.

Mouse and human BCCs respond to MKL1 inhibitors *in vivo*

Our human tissue and *in vitro* data suggest that resistant tumors have evolved to activate a RhoA–mDia–actin–SRF–MKL1 pathway to potentiate GLI-dependent signaling and BCC growth. To determine the therapeutic potential of this pathway, we investigated allografts of rBCCs generated from PTC53-BCC mice (**Fig. 1**) after treatment
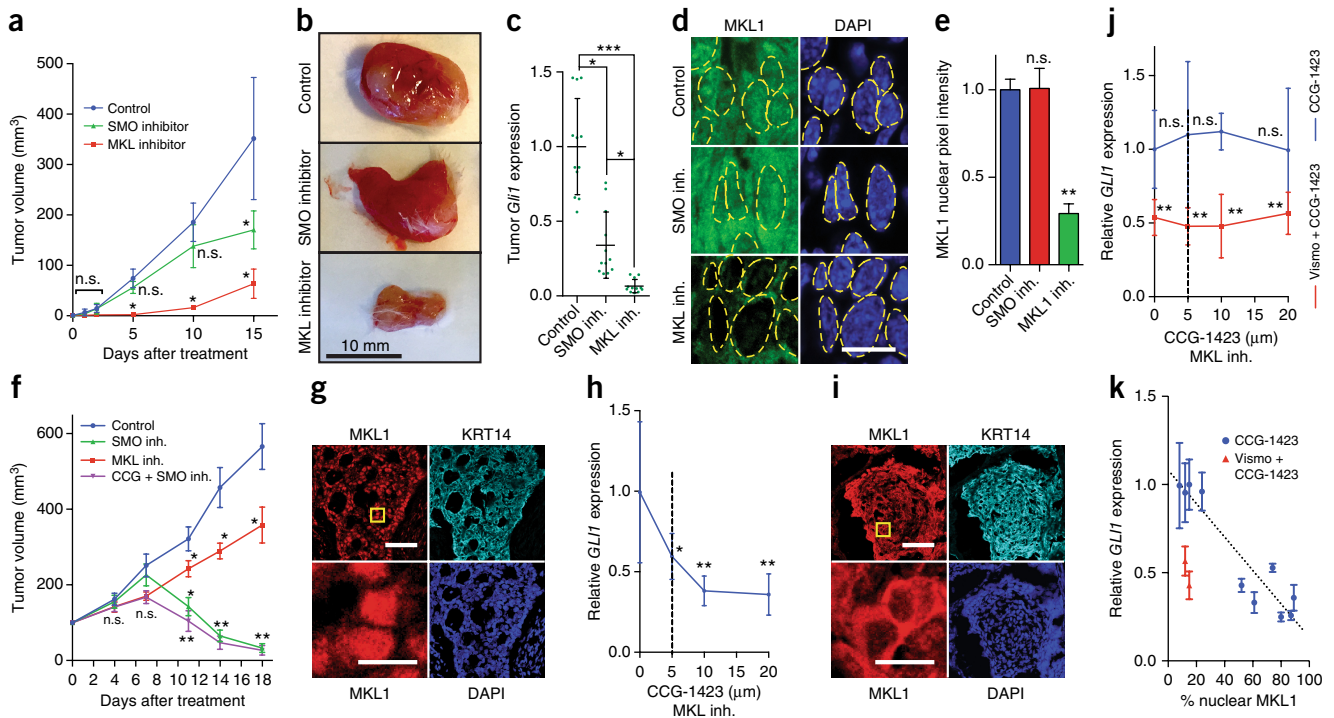
Figure 6 Pharmacological inhibition of MKL1 produces an *in vivo* therapeutic response in mouse and human BCCs. (**a**) Resistant tumor growth (parental tumor 1) following treatment with SMO inhibitor (vismodegib; intraperitoneal (i.p.), 100 mg per kg body weight), MKL inhibitor (CCG-203971; i.p., 100 mg per kg body weight), or vehicle control (DMSO) via i.p. injection. A Student's *t*-test was used to determine the change in drug-treated tumor volume relative to vehicle control. *$P < 0.05$. $n = 4$ tumors for each condition. Data are repeated in **Supplementary Figure 15** using a distinct parental tumor line. (**b**) Representative tumors after treatment with the indicated inhibitor. (**c**) Results from qPCR performed to measure *Gli1* mRNA expression in resistant mouse tumors treated with the indicated inhibitors ($n = 12$ tumors per condition). A Student's *t*-test was used to compare indicated treatment versus vehicle control. *$P < 0.05$, ***$P < 0.001$. (**d**) Immunofluorescence staining for MKL1 showing cytoplasmic localization in CCG-203971-treated tumor sections; DAPI marks nuclei. The yellow dashed lines highlight cell nuclei. Scale bar, 10 μm. (**e**) Quantification of MKL1 nuclear pixel intensity in tumors from **d** treated with the indicated inhibitors ($n = 100$ cells per condition). **$P < 0.01$. A Student's *t*-test was used to compare indicated treatment versus vehicle control. (**f**) Tumor volume of drug-naive mouse tumors following treatment with vehicle control (DMSO), CCG-203971 (i.p., 100 mg per kg body weight), SMO inhibitor (XL139, oral gavage 25 mg per kg body weight), or the indicated combination. *$P < 0.05$, **$P < 0.01$. A Student's *t*-test was used to compare indicated treatment versus vehicle control. (**g,i**) Representative immunofluorescence fields highlighting variable nuclear localization (**g**) and cytoplasmic accumulation (**i**) of MKL1 in human advanced BCC tumor explants. Ten consecutive fresh surgical specimens were stained. KRT14 marks tumor area and DAPI marks nuclei in each field. Scale bars in **g** and **i**, 50 μm and 10 μm in low- and high-magnification fields, respectively. (**h**) Results from qPCR showing *GLI1* expression in the treated tumor in **g**. A Student's *t*-test was used to compare individual data points versus vehicle control. *$P < 0.05$, **$P < 0.01$. (**j**) Results from qPCR showing the change in *GLI1* expression in response to the indicated treatments. A Student's *t*-test was used to compare individual data points versus vehicle control. **$P < 0.01$. (**k**) Relative *GLI1* expression in response to MKL1 inhibition (blue circles) or SMO inhibition (red triangles) determined through qPCR ($n = 10$ tumors). The best-fit linear regression line (black dotted line) is shown to highlight the relationship between nuclear MKL1 and *GLI1* response following MKL1 inhibition. Data in **a**, **c**, **f**, **h**, **j**, and **k** represent means ± s.e.m.; data in **e** represent mean + s.e.m.

with the MKL1 inhibitor CCG-203971, which has recently been shown to have *in vivo* tolerability[33,34]. Consistent with our *in vitro* growth data, systemic MKL1 inhibition caused a dramatic decline in resistant tumor growth *in vivo* as compared to SMO inhibition in two independent parental tumor lines (**Fig. 6a,b** and **Supplementary Fig. 15**). MKL1 inhibitors caused significantly reduced levels of *GLI1* expression (**Fig. 6c**), reflecting the dependence of our mouse resistant tumors on the hedgehog pathway. SMO inhibition also caused a reduction in *GLI1* expression; however, *GLI1* depletion did not reach the threshold necessary for disease response (**Fig. 6c**), which is consistent with reports of moderate *GLI1* inhibition accompanying the limited response in patients with rBCCs treated with arsenic trioxide and itraconazole[35]. The MKL1 inhibitor, but not vismodegib, prevented MKL1 recruitment into the nucleus of tumor cells and caused a reduction in proliferation (**Fig. 6d,e** and **Supplementary Fig. 16**). As sBCCs contain mainly cytoplasmic MKL, we predicted that they

would respond to SMO inhibition but not to MKL1 inhibitors. Indeed, sBCCs and sensitive cell lines responded to SMO inhibitors but only weakly to CCG-203971 (**Fig. 6f** and **Supplementary Fig. 17**), suggesting that MKL1 dependence predominates in rBCCs but not in sBCCs. Thus, we conclude that systemic treatment with MKL1 inhibitors considerably improves tumor outcome as compared to treatment with SMO inhibitors in rBCCs.

To determine the therapeutic potential of MKL1 inhibitors in advanced human BCCs and because of the inability to generate patient-derived xenografts (PDXs), we developed tumor explant culture conditions for ten consecutive freshly resected advanced BCCs from human subjects. In contrast to simple BCCs, advanced BCCs are naive to SMO inhibitors but regularly exhibit partial resistance at the time of treatment[10,36]. We measured *GLI1* transcript levels in RNA extracts from tumor explants containing nuclear MKL1; we observed a significant reduction in *GLI1* expression in MKL-inhibitor-treated tumors relative to vehicle-treated

controls (**Fig. 6g,h** and **Supplementary Fig. 18**), suggesting that MKL1 inhibition may provide a therapeutic benefit in this subset of patients. Similar to the naive mouse tumors, human tumors containing inactive cytoplasmic MKL1 did not respond to CCG-1423 (**Fig. 6i,j** and **Supplementary Fig. 18g–l**), indicating that MKL1 inhibition has a limited therapeutic benefit in this subset of tumors. Notably, treatment with the SMO inhibitor vismodegib produced a robust *GLI1* response in two independent tumors with cytoplasmic MKL1 (**Fig. 6j** and **Supplementary Fig. 18i,l**). Further quantification of MKL1 compartmentalization revealed a strong correlation between MKL1 nuclear accumulation and the response to MKL1 inhibitors in human tumor explants (**Fig. 6k**). We conclude that MKL1 inhibition has *in vivo* efficacy in mouse rBCCs and human tumor explants. Our results uncover a previously unknown mechanism through which the Rho kinase–MKL1–SRF pathway activates GLI1 activity, causing resistance, and demonstrate that inhibitors of this pathway provide a promising therapeutic avenue for patients with rBCCs.

DISCUSSION

Results from our tumor sequencing and histologic studies in human BCC samples highlight SRF–MKL1 activation as a dominant driver of growth in the majority of rBCCs and validate the initial results from our mouse model of resistance. We reveal that SRF–MKL1 acts as a new activator of the hedgehog signaling pathway by potentiating GLI1 transcriptional activity. Additionally, our studies demonstrate antitumor activity for MKL1 inhibitors in both human tumor explants and in our mouse model of resistance, providing preclinical justification to add MKL1 as a new therapeutic target to the cancer armamentarium.

We demonstrate that nuclear (activated) MKL1 is present in the majority of rBCCs (**Fig. 4**), implicating active MKL1 as a dominant driver of tumor resistance. It should be noted that tumor burden was reduced in sensitive mouse tumors treated with the MKL inhibitor (Student's *t*-test for treatment versus control at days 11, 14, and 18, $P < 0.05$); however, the effect was much more pronounced with SMO inhibitor treatment in these naive tumors (**Fig. 6f**). This suggests a small amount of tumor heterogeneity in drug-naive mouse tumors. In fact, six out of ten highly advanced human naive BCCs displayed high levels of nuclear MKL1 (**Fig. 6k**), suggesting that this pathway plays a major role in innate BCC resistance, which is present in ~60% of advanced drug-naive BCCs[36]. We knocked down expression of additional RPEL proteins (PHACTR1 and KDM3A) and observed no change in hedgehog pathway activity (**Supplementary Fig. 19**), suggesting that MKL is unique among RPEL proteins with respect to hedgehog pathway modulation. Our GSEA data indicate that SRF is activated only in human tumors that do not contain *SMO* mutations (**Fig. 2g**). Notably, we demonstrate that this 'nuclear MKL1 patient group' responds favorably to MKL1 inhibitors by reducing *GLI1* expression (**Fig. 6k**). Our initial study demonstrated predominantly cytoplasmic MKL1 in sporadic human BCCs, with a few small regions containing nuclear MKL1 (**Fig. 4f** and data not shown). However, nuclear MKL1 appears to be enriched in highly advanced naive BCCs from humans (**Fig. 6k**) and further enriched in cases resistant to SMO inhibitors (**Fig. 4g**). Thus, tumor heterogeneity with respect to MKL1 nuclear localization underpins the need to define patient subtype to inform therapeutic outcome.

Our observation that GLI1 binds near, but not directly at, the center of the SRF enrichment profile suggests that these TFs may exist as part of a large TF complex. In accordance with this hypothesis, GLI1, SRF, and MKL1 form a complex (**Fig. 2h,i**); however,

GLI1 and SRF chromatin binding sites do not overlap directly, suggesting that they interact indirectly through undiscovered complex members found at common gene loci (**Fig. 3l** and **Supplementary Fig. 20**). Additionally, GLI1 directs SRF occupancy at GLI-bound target sites (**Fig. 3n**), which is consistent with previous work indicating that SRF target specificity is determined by its binding partners[17,19]. We did not observe a change in MKL1 compartmentalization upon GLI1 inhibition (**Supplementary Fig. 21**), suggesting that GLI1 recruits MKL through an intranuclear mechanism. We detected the PLA signal using GLI1 and SRF antibodies (**Supplementary Figs. 3** and **4**); however, we did not observe the PLA signal for GLI1 and MKL1 (data not shown). This observation suggests closer proximity for GLI1–SRF protein binding compared to GLI1–MKL1; however, both SRF and MKL1 exist in a complex with GLI1 (**Fig. 2h,i**). The GLI1 target binding identified in this study (**Fig. 3m,n**) was not observed in previous SRF and MKL1 ChIP–seq data sets[37,38]. However, ENCODE data sets do contain SRF ChIP signals at both hedgehog targets and other oncogenic promoters in tumor, but not normal, tissues (**Supplementary Fig. 22**), illustrating how SRF recruitment through GLI1 further broadens its genomic binding capabilities in the context of tumor resistance. The necessity for GLI1 recruitment comes from the finding that Rho–mDIA–SRF–MKL1 activity is not sufficient to induce *GLI1* expression (**Figs. 3g** and **5g**), and SRF–MKL1 does not activate the other TF pathways we examined in BCCs (data not shown). A recent report highlighted an interaction between MKL1 and JMJD1A that destabilized GLI1 at the protein level and caused suppression of hedgehog pathway activation[39]. However, JMJD1A is not expressed in human or mouse BCCs, indicating that rBCCs have evaded this GLI1 protein stabilization mechanism.

Our study provides a strong physiological connection between tumorigenic hedgehog signaling and SRF–MKL1 that has not been explored previously, to our knowledge. Emerging studies on the role of hedgehog signaling in the fibrotic response of scleroderma[40], along with the established role of SRF–MKL1 in inflammation, suggest that rBCCs, although expressing canonical keratinocyte markers, have acquired characteristics of myofibroblasts. Previous studies have attributed cytoskeletal alteration in tumor progression to the increased mobility and deformability of activated cells[41]. Moreover, Rho activation is known to increase metastatic ability through the actin cytoskeleton and indirectly through SRF–MKL1 activation[20,42]. Our human and mouse RNA-seq data highlight an upregulation of genes involved in integrin activation (**Supplementary Fig. 2d,e**), a known activation pathway upstream of Rho. Our data are consistent with findings from a recent study that compared human BCCs to healthy skin, uncovering integrin activation as the most highly enriched pathway term[23]. This suggests that many sporadic BCCs from humans have upregulated adhesion signaling, which may play a role in the 50–70% of patients who develop resistance[36]. Integrin activation likely results from changes within the extracellular matrix, suggesting that the tumor microenvironment plays an important role in growth of drug-resistant tumors. The observation that BCCs do not grow in PDXs further suggests a role for the tumor stroma in BCC viability. In our study, we addressed this by developing culture conditions for patient-derived explants (**Fig. 6g–k**). Efforts to improve culture conditions to facilitate additional assays (for example, growth assays) are ongoing. Our finding that mDia, but not ROCK, is required downstream of Rho for rBCC growth (**Fig. 5d–f**) adds an additional mechanistic detail and potential therapeutic target for treatment of patients refractory to SMO inhibitors. A previous study describes an inhibitory

role for mDia1 in DYRK1A-dependent GLI transcription[43]. We found that mDia promoted GLI-dependent transcription (**Fig. 5g**), suggesting that DYRK1A and Rho stimulate mDia to produce opposing outcomes on the hedgehog pathway. How mDia promotes these opposing outcomes is an important area for future investigation. Taken together, our results suggest that the tumor microenvironment provides progrowth signaling to promote cytoskeletal remodeling and resistance to targeted therapies through potentiating GLI signaling (**Supplementary Fig. 23**).

This study uncovers a potent and exciting therapeutic target for future cancer treatment. Our multicomponent genomic analyses highlight SRF and MKL1 as new activators of hedgehog-dependent transcription, and we utilize this finding to target MKL1 with pharmacological inhibitors to treat rBCCs. Our *in vivo* mouse (**Fig. 6a**–**f**) and human tumor explant (**Fig. 6g**–**k**) data highlight the therapeutic potential for MKL1 inhibitors in human BCCs. Previous studies have focused on the role of SRF–MKL1 in inflammation[44]; however, our work provides preclinical justification to extend MKL1 inhibitors to oncogenic therapy. The demonstration that SRF–MKL1 can potentiate oncogenic driver pathways opens the possibility of using MKL1 inhibitors as a therapeutic in other tumor types. The activities of MKL1 inhibitors and SMO inhibitors are likely to synergize when used in conjunction given the parallel nature of these signaling pathways in BCCs; thus, combination therapy will be a major focus as these inhibitors move toward clinical development.

METHODS

Methods, including statements of data availability and any associated accession codes and references, are available in the online version of the paper.

Note: Any Supplementary Information and Source Data files are available in the online version of the paper.

AUTHOR CONTRIBUTIONS

R.J.W. and A.E.O. designed the experiments and wrote the manuscript. R.J.W. performed the majority of experiments. A.L. performed all mouse tumor generation experiments except for rBCC drug treatment experiments with vismodegib and CCG-203971, which were administered by R.J.W. CCG-203971 *in vivo* drug treatment was repeated by M.A.F. The majority of cellular and molecular experiments were assisted and optimized by N.M.U. Exome- and RNA-seq analyses were carried out by J.R.L. and G.S. Co-IP experiments were carried out by A.M. C.Y.Y. assisted with SRF and MKL1 inhibition studies and knockdown studies as well as RHO and mDia experiments. S.X.A. assisted with RNA- and exome-seq library generation. S.Z.A., S.T.H., and K.Y.S. provided human tumor samples and annotation. E.H.E. and J.Y.T. designed the PTC53-BCC mouse resistance model. A.S.B., M.P.S., and E.Y.L. provided GLI ChIP data.

1. Junttila, M.R. & de Sauvage, F.J. Influence of tumour micro-environment heterogeneity on therapeutic response. *Nature* **501**, 346–354 (2013).
2. Ransohoff, K.J., Tang, J.Y. & Sarin, K.Y. Squamous change in basal-cell carcinoma with drug resistance. *N. Engl. J. Med.* **373**, 1079–1082 (2015).
3. Atwood, S.X., Whitson, R.J. & Oro, A.E. Advanced treatment for basal cell carcinomas. *Cold Spring Harb. Perspect. Med.* **4**, a013581 (2014).
4. Amaral, L. *et al.* Inhibitors of bacterial efflux pumps that also inhibit efflux pumps of cancer cells. *Anticancer Res.* **32**, 2947–2957 (2012).
5. Thomas-Schoemann, A. *et al.* Drug interactions with solid tumour–targeted therapies. *Crit. Rev. Oncol. Hematol.* **89**, 179–196 (2014).
6. Nürnberg, A., Kitzing, T. & Grosse, R. Nucleating actin for invasion. *Nat. Rev. Cancer* **11**, 177–187 (2011).
7. Barker, H.E., Paget, J.T., Khan, A.A. & Harrington, K.J. The tumour microenvironment after radiotherapy: mechanisms of resistance and recurrence. *Nat. Rev. Cancer* **15**, 409–425 (2015).
8. McMillin, D.W., Negri, J.M. & Mitsiades, C.S. The role of tumour–stromal interactions in modifying drug response: challenges and opportunities. *Nat. Rev. Drug Discov.* **12**, 217–228 (2013).
9. Basset-Seguin, N., Sharpe, H.J. & de Sauvage, F.J. Efficacy of hedgehog pathway inhibitors in basal cell carcinoma. *Mol. Cancer Ther.* **14**, 633–641 (2015).
10. Sekulic, A. *et al.* Efficacy and safety of vismodegib in advanced basal-cell carcinoma. *N. Engl. J. Med.* **366**, 2171–2179 (2012).
11. Chang, A.L. & Oro, A.E. Initial assessment of tumor regrowth after vismodegib in advanced basal cell carcinoma. *Arch. Dermatol.* **148**, 1324–1325 (2012).
12. Atwood, S.X. *et al.* Smoothened variants explain the majority of drug resistance in basal cell carcinoma. *Cancer Cell* **27**, 342–353 (2015).
13. Sharpe, H.J. *et al.* Genomic analysis of smoothened inhibitor resistance in basal cell carcinoma. *Cancer Cell* **27**, 327–341 (2015).
14. Atwood, S.X., Li, M., Lee, A., Tang, J.Y. & Oro, A.E. GLI activation by atypical protein kinase C ι/λ regulates the growth of basal cell carcinomas. *Nature* **494**, 484–488 (2013).
15. Atwood, S.X. *et al.* Rolling the genetic dice: neutral and deleterious smoothened mutations in drug-resistant basal cell carcinoma. *J. Invest. Dermatol.* **135**, 2138–2141 (2015).
16. Zaromytidou, A.I., Miralles, F. & Treisman, R. MAL and ternary complex factor use different mechanisms to contact a common surface on the serum response factor DNA-binding domain. *Mol. Cell. Biol.* **26**, 4134–4148 (2006).
17. Wang, Z. *et al.* Myocardin and ternary complex factors compete for SRF to control smooth muscle gene expression. *Nature* **428**, 185–189 (2004).
18. Marais, R., Wynne, J. & Treisman, R. The SRF accessory protein Elk-1 contains a growth factor–regulated transcriptional activation domain. *Cell* **73**, 381–393 (1993).
19. Janknecht, R. & Nordheim, A. Elk-1 protein domains required for direct and SRF-assisted DNA-binding. *Nucleic Acids Res.* **20**, 3317–3324 (1992).
20. Miralles, F., Posern, G., Zaromytidou, A.I. & Treisman, R. Actin dynamics control SRF activity by regulation of its coactivator MAL. *Cell* **113**, 329–342 (2003).
21. Wang, G.Y. *et al.* Establishment of murine basal cell carcinoma allografts: a potential model for preclinical drug testing and for molecular analysis. *J. Invest. Dermatol.* **131**, 2298–2305 (2011).
22. Webster, D.E. *et al.* Enhancer-targeted genome editing selectively blocks innate resistance to oncokinase inhibition. *Genome Res.* **24**, 751–760 (2014).
23. Bonilla, X. *et al.* Genomic analysis identifies new drivers and progression pathways in skin basal cell carcinoma. *Nat. Genet.* **48**, 398–406 (2016).
24. Olson, E.N. & Nordheim, A. Linking actin dynamics and gene transcription to drive cellular motile functions. *Nat. Rev. Mol. Cell Biol.* **11**, 353–365 (2010).
25. Heidenreich, O. *et al.* MAPKAP kinase 2 phosphorylates serum response factor *in vitro* and *in vivo*. *J. Biol. Chem.* **274**, 14434–14443 (1999).
26. Zhang, H.M. *et al.* Mitogen-induced recruitment of ERK and MSK to SRE promoter complexes by ternary complex factor Elk-1. *Nucleic Acids Res.* **36**, 2594–2607 (2008).
27. Blaker, A.L., Taylor, J.M. & Mack, C.P. PKA-dependent phosphorylation of serum response factor inhibits smooth muscle–specific gene expression. *Arterioscler. Thromb. Vasc. Biol.* **29**, 2153–2160 (2009).
28. Pawłowski, R., Rajakylä, E.K., Vartiainen, M.K. & Treisman, R. An actin-regulated importin α/β-dependent extended bipartite NLS directs nuclear import of MRTF-A. *EMBO J.* **29**, 3448–3458 (2010).
29. Mokady, D. & Meiri, D. RhoGTPases—a novel link between cytoskeleton organization and cisplatin resistance. *Drug Resist. Updat.* **19**, 22–32 (2015).
30. Guettler, S. *et al.* RPEL motifs link the serum response factor cofactor MAL but not myocardin to Rho signaling via actin binding. *Mol. Cell. Biol.* **28**, 732–742 (2008).
31. Li, F. & Higgs, H.N. The mouse Formin mDia1 is a potent actin nucleation factor regulated by autoinhibition. *Curr. Biol.* **13**, 1335–1340 (2003).

32. Rath, N. & Olson, M.F. Rho-associated kinases in tumorigenesis: re-considering ROCK inhibition for cancer therapy. *EMBO Rep.* **13**, 900–908 (2012).

33. Haak, A.J. *et al.* Targeting the myofibroblast genetic switch: inhibitors of myocardin-related transcription factor/serum response factor–regulated gene transcription prevent fibrosis in a murine model of skin injury. *J. Pharmacol. Exp. Ther.* **349**, 480–486 (2014).

34. Sisson, T.H. *et al.* Inhibition of myocardin-related transcription factor/serum response factor signaling decreases lung fibrosis and promotes mesenchymal cell apoptosis. *Am. J. Pathol.* **185**, 969–986 (2015).

35. Ally, M.S. *et al.* Effects of combined treatment with arsenic trioxide and itraconazole in patients with refractory metastatic basal cell carcinoma. *JAMA Dermatol.* **152**, 452–456 (2016).

36. Sekulic, A. *et al.* Pivotal ERIVANCE basal cell carcinoma (BCC) study: 12-month update of efficacy and safety of vismodegib in advanced BCC. *J. Am. Acad. Dermatol.* **72**, 1021–1026. e8 (2015).

37. Vasudevan, H.N. & Soriano, P. SRF regulates craniofacial development through selective recruitment of MRTF cofactors by PDGF signaling. *Dev. Cell* **31**, 332–344 (2014).

38. Esnault, C. *et al.* Rho–actin signaling to the MRTF coactivators dominates the immediate transcriptional response to serum in fibroblasts. *Genes Dev.* **28**, 943–958 (2014).

39. Schneider, P. *et al.* Identification of a novel actin-dependent signal transducing module allows for the targeted degradation of GLI1. *Nat. Commun.* **6**, 8023 (2015).

40. Horn, A. *et al.* Hedgehog signaling controls fibroblast activation and tissue fibrosis in systemic sclerosis. *Arthritis Rheum.* **64**, 2724–2733 (2012).

41. Parri, M. & Chiarugi, P. Rac and Rho GTPases in cancer cell motility control. *Cell Commun. Signal* **8**, 23 (2010).

42. Jiang, P., Enomoto, A. & Takahashi, M. Cell biology of the movement of breast cancer cells: intracellular signalling and the actin cytoskeleton. *Cancer Lett.* **284**, 122–130 (2009).

43. Morita, K., Lo Celso, C., Spencer-Dene, B., Zouboulis, C.C. & Watt, F.M. HAN11 binds mDia1 and controls GLI1 transcriptional activity. *J. Dermatol. Sci.* **44**, 11–20 (2006).

44. Johnson, L.A. *et al.* Novel Rho/MRTF/SRF inhibitors block matrix-stiffness and TGF-β-induced fibrogenesis in human colonic myofibroblasts. *Inflamm. Bowel Dis.* **20**, 154–165 (2014).

ONLINE METHODS

Subject case samples. Written informed consent was obtained for all human subject samples and was reviewed by the Stanford University Institutional Review Board. rBCCs and sBCCs were defined using the Response Evaluation Criteria in Solid Tumors (RECIST) method. BCC tumors that exhibited progressive or stable growth following continuous treatment with vismodegib (150 mg per day) were defined as resistant tumors. BCCs exhibiting partial or complete regression with vismodegib treatment (150 mg per day) were defined as sensitive tumors, as defined by RECIST.

***Ptch*^{+/−}; KRT14-Cre-ER; *Trp53*^{fl/fl} mice.** All mice were housed under standard conditions, and animal care was in compliance with the protocols approved by the Institutional Animal Care and Use Committee (IACUC) at Children's Hospital Oakland Research Institute (CHORI) and Stanford University. PTC53-BCC mice were generated and used to generate BCC tumors as described previously[21,45]. Here we exposed mice to irradiation (5 Gy) using an X-ray irradiator. To generate resistant tumors, initial tumors from PTC53-BCC mice were passaged into NOD-SCID mice as described in the original PTC53-BCC model. NOD-SCID mice were then treated with the Smo inhibitor GDC-619 after tumors reached 100 mm³ in volume. Mice received three treatments of Smo inhibitor over 10 d before cessation of inhibitor treatment. Regressed tumors were allowed to grow without inhibitor for 20 d before treatment with another round of the Smo inhibitor as described above. Growth and inhibitor cycles were repeated until tumors became resistant to the Smo inhibitor (continued growth in the presence of GDC-619). An average of three growth–inhibitor-treatment cycles were required to produce resistant tumors. For *in vivo* validation of MKL1 inhibition, resistant tumors were generated in NOD-SCID mice using the method outlined above. To account for differences in growth rates between parental resistant tumors, we passaged each parental tumor into additional NOD-SCID mice so that drug treatment and vehicle control were compared between mice seeded with a common parental tumor (n = 3 tumors per mouse). Mice received drug treatment via i.p. injection daily for 15 d using 100 mg CCG203971 (Cayman Chemical) and/or vismodegib (Selleckchem) per kg body weight. Treatment was administered starting at the time of tumor passage for both CCG203971 and vismodegib. The SMO inhibitor XL-139 (25 mg per kg body weight) was administered by oral gavage every 48 h to NOD-SCID mice with BCC allografts for initial resistant tumor generation and drug treatment in drug-naive BCCs (**Fig. 6f**).

Mouse whole-exome tumor sequencing. Exome-seq of mouse tumors was carried out using tissue frozen in RNAlater (Ambion) at −80 °C. Tumor DNA was isolated using the DNeasy Blood & Tissue Kit (Qiagen). Exome capture was performed with the Agilent SureSelectXT kit using 2 µg of DNA. Paired-end 100-bp reads were generated using isolated whole exomes sequenced on the Illumina HiSeq 2500 platform. Our exome-seq pipeline produced a mean coverage of 195× within coding regions. Sequencing reads were aligned to the mouse reference genome sequence (mm9) using Burrows–Wheeler Aligner. SAM file to BAM file conversion was carried out using Picard tools, and local realignment around indels with base-quality-score recalibration was performed using the Genome Analysis Toolkit (GATK). Single-nucleotide variants (SNVs) were called using GATK. The annotation of nonsynonymous SNVs was performed using Annovar. Comparison to the human BCC mutational landscape was performed using previously published variants[12]. *Smo* mutation was identified through calling variants on unfiltered alignment files using SAMtools and was annotated through SnpEff using the GRCm38.71 genome.

RNA sequencing and bioinformatic screening. Library preparation, sequencing, and mapping were carried out as described previously[12] with minor modifications. Alignment was performed using TopHat with mm9 as a reference genome. The DEseq R package was used to create a preranked list of genes differentially expressed in resistant versus sensitive tumors, and this list was used to perform GSEA (Broad Institute) using the TRANSFAC database for TF targets. Enriched TFs were ranked according to the FDR determined from GSEA; this is presented in **Figure 2**. An additional GSEA was carried out using

RNA-seq data from published human rBCCs (n = 6) and sBCCs (n = 4)[12], which were ranked according to FDR score, as described above. Pathway enrichment terms from RNA-seq data were obtained using Enrichr[46].

GLI1 ChIP–seq data were obtained from mouse embryonic central nervous system[47], mouse granular neural progenitors (GNPs; **Supplementary Fig. 2c**) and medulloblastoma (**Fig. 2a,c**; unpublished data), and an additional data set of mouse GNPs[48]. GLI3 ChIP–seq data were obtained from mouse embryonic limb bud[49].

TFs sharing occupancy sites with GLI1 and GLI3 were identified using FOCIS, as described previously[22]. FOCIS pattern matches TF binding signatures from chromosomal interval data (GLI1 ChIP–seq in our case) with the curated data sets from ENCODE, TRANSFAC, JASPER, Swiss Regulon, HOCOMOCO, and UCSC Conserved TFBS databases. To determine enrichment at GLI1 or GLI3 binding sites, subset and background data sets were generated using GLI1 or GLI3 ChIP–seq data. Putative GLI1 cofactors were ranked according to FOCIS enrichment (Z-score). Enrichment scores were generated through conversion of Z-scores to a scale between 0 and ±1. Multidimensional genomic analysis was performed through plotting GSEA rank and FOCIS enrichment along the x and y axis, respectively (**Fig. 2c**). Additional multidimensional analyses were carried out using GSEA data from human RNA-seq read values as described above. GSEA enrichment scores for SRF were obtained for individual human resistant tumors by running the GSEA algorithm for each resistant tumor compared to the mean sequencing values for all sensitive tumors in the data set.

Chromatin immunoprecipitation. Protein–DNA complexes were isolated from ASZ001 cells, and these were used to map chromatin occupancy of endogenous SRF, as described previously[48] with minor modifications. Cells were cross-linked with 1% formaldehyde for 10 min. Cells were lysed in modified RIPA buffer (50 mM Tris, 150 mM NaCl₂, 1% Triton X-100, 0.75% SDS, 0.5% sodium deoxycholate), which was supplemented with protease and phosphatase inhibitor cocktail (Roche). Cellular extracts were sonicated using a Covaris B208 ultrasonicator to produce chromatin fragments 100–400 bp in length. Cleared extract was incubated with 5 µg of antibody against SRF (Santa Cruz) or nonspecific IgG control antibody (Cell Signaling) overnight and precipitated using Protein A/G Sepharose beads. Beads were washed with ChIP wash buffer (100 mM Tris pH 9.0, 500 mM LiCl, 1% IGEPAL, 1% deoxycholic acid, protease inhibitor cocktail (Roche)) and protein–DNA complexes were eluted with IP elution buffer (1% SDS, 50 mM NaCOH₃). Cross-links were reversed by incubation at 67 °C overnight while shaking at 1,400 r.p.m. on a thermoshaker. RNA was digested with 0.2 µg/ml RNase A at 37 °C for 30 min. DNA was isolated using Qiagen MinElute columns following the manufacturer's instructions. The relative fold enrichment of SRF was determined via adding DNA to the Brilliant II SYBR Green qPCR Master Mix Kit (Agilent Technologies). Data from ChIP with a nonspecific IgG control antibody incubated with the ASZ001 extract were used as a control in calculation of fold enrichment.

ChIP–seq libraries were generated using the standard protocol for the NEBNext Ultra II DNA Library Prep Kit for Illumina (New England BioLabs). ChIP libraries were sequenced using the Illumina HiSeq 4000 platform. Alignment was carried out using TopHat with mm9 as a reference genome. High-confidence peaks were obtained using MACS2 (P < 0.0001; dynamic Poisson distribution). Background removal was carried out via submitting replicates to irreproducible discovery rate (IDR) filtering. DEseq was used to determine enrichment at GLI1 and SRF peaks. The heatmap and histogram were generated using the annotatePeaks.pl script in the Homer suite as described previously[50]. Heatmap data were visualized using Java TreeView. Read pileups at genomic loci were imaged using Integrated Genomics Viewer (Broad Institute). High-confidence peaks were annotated for gene associations using the Genomic Regions Enrichment of Annotations Tool (GREAT)[51].

Immunofluorescence. BCC tumors were fixed with 4% paraformaldehyde and embedded in paraffin blocks. 5-µm sections were mounted onto glass slides and stained with H&E or were immunolabeled using the antibodies listed below. Cells plated in 8-well chamber slides (Millipore) were fixed using 3.7% formaldehyde

diluted in PBS for 10 min. Sections or chamber slides were immunostained using a previously described protocol (Cell Signaling Technologies IF General Protocol; https://www.cellsignal.com/contents/resources-protocols/immunofluorescence-general-protocol/if) using the following antibodies and dilutions: anti-SRF (1:100, Santa Cruz Biotechnology, sc-335; **Supplementary Fig. 24**), anti–keratin 14 (1:500, Abcam, ab130102), anti-GLI1 (1:100, R&D Systems, AF3455; **Supplementary Fig. 25**), anti-MKL1 (1:200, Sigma, HPA030782; **Supplementary Fig. 26**), anti-β-tubulin (1:500, DSHB, E7), and anti-Ki-67 (1:1,000, Abcam, ab15580). The fluorescent-labeled secondary antibodies used were as follows: anti–goat Alexa Fluor 488 (1:500, Life Technologies, A-11055), anti–mouse Alexa Fluor 488 (1:500, Life Technologies, A-21202), anti–rabbit Alexa Fluor 555 (1:500, Life Technologies, A-31572), anti–mouse Alexa Fluor 594 (1:500, Life Technologies, A-21203), and anti–chicken Alexa Fluor 647 (1:500, Jackson Immuno Research, 703-606-155). Confocal imaging was carried out using a Leica SP8 microscope equipped with an adjustable white light laser and hybrid detectors. To quantify *GLI1* expression in BCCs (**Fig. 1**), pixel intensity was measured using ImageJ in regions that stained positive for keratin 14. For each condition (sensitive and resistant), 3 fields were counted in 5 independent tumors for a total of 15 data fields per condition. Subcellular localization of SRF and MKL1 (**Fig. 2**) was quantified through multiposition intensity profiles using the ImageJ multi-plot plug in. Keratin 14 and DAPI staining were used as guides to determine cytoplasmic and nuclear localization, respectively. The percentage of cells staining positive for nuclear MKL1 in human BCCs was quantified through flash freezing tumor fragments and embedding them in optimum cutting temperature (O.C.T.) compound for cryosectioning. Nuclear MKL1 was quantified using DAPI as a guide for nuclei and KRT14 as a guide for tumor area. Actin filament staining was carried out using phalloidin 488 and 647 (Life Technologies).

Proximity ligation assay (PLA) staining was carried out using co-labeling with primary antibodies against GLI1 (raised in goat) with SRF (raised in rabbit), GLI1 with MKL1 (raised in rabbit), and GLI1 with non-specific rabbit IgG (Cell Signaling). Secondary antibodies consisted of Duolink goat plus (Sigma, DUO92003) and rabbit minus (Sigma, DUO92005). Detection of complexes was carried out using Duolink Red *in situ* reagents (Sigma, DUO92008).

Immunoblotting. Whole-cell extracts were harvested using RIPA buffer supplemented with protease and phosphatase inhibitors (Roche), run on SDS–PAGE gels (Life Technologies), and then transferred onto nitrocellulose membranes. To prepare nuclear extracts, cells were resuspended in hypotonic lysis buffer (10 mM HEPES pH 7.9, 1.5 mM MgCl$_2$, and 10 mM KCl) and dounced 15 times. Isolated nuclei were pelleted and resuspended in RIPA buffer. Immunoblotting was carried out using antibodies against the following proteins: GLI1 (Cell Signaling, 2534) (**Supplementary Fig. 27**), β-tubulin (Developmental Studies Hybridoma Bank, E7), Flag M2 (Sigma, F1804), HA (Abcam, ab9110) (**Supplementary Fig. 28**), GAPDH (Santa Cruz, sc-365062, histone H3 (Abcam, ab1791), SRF (Santa Cruz, sc-335), and MKL1 (Novus, NBP1-88498). All immunoblots were imaged using the LI-COR Odyssey image system.

Cell culture. ASZ001 and BSZ001 BCC cells were cultured in 154CF medium (Life Technologies) supplemented with 2% chelated FBS and 0.05 mM CaCl$_2$. Experiments were carried out using low serum conditions with 154CF medium containing 0.2% chelated FBS and 0.05 mM CaCl$_2$. NIH-3T3, HaCaT, and HEK-293T cells were cultured in DMEM supplemented with 10% FBS. Hedgehog induction experiments were carried out using low-serum DMEM containing 0.5% FBS. UW-BCC1 cells (human BCC cells) were isolated from an individual with a superficial BCC. Cells were cultured as described previously[52].

Coimmunoprecipitation. Expression of N-terminally tagged Flag-GLI1 and HA-SRF was carried out in HEK-293T cells using the pCS2 backbone. Transiently transfected cells were harvested from 80% confluent 10-cm plates. Lysis buffer consisted of Tris-buffered saline pH 7.4, 1% Triton X-100, and protease inhibitor cocktail (Sigma). Cleared lysates were incubated overnight with Flag M2 magnetic beads (Sigma), HA magnetic beads (Thermo Fisher), or IgG control beads (Thermo Fisher). Protein was eluted in 50 μl RIPA buffer containing protease inhibitor cocktail. Additional pulldown experiments were carried out using the

TnT SP6 Quick Coupled Transcription/Translation System (Promega). Expression of Flag-GLI1, HA-SRF, and C-terminally Myc-tagged MKL1 (Myc-MKL1) was carried out using the pCS2 backbone. Tagged MKL1 was pulled down using anti-c-Myc magnetic beads (Thermo Fisher). Cell-free extracts were eluted after pulldown using 50 μl of RIPA supplemented with protease inhibitor cocktail. All pulldown extracts were immunoblotted using the method described above.

SRF knockdown and inhibitor treatment. Knockdown of SRF was achieved through lentiviral transduction using shRNAs expressed in the pLKO.1 backbone (Open Biosystems). Cell growth assays were performed through plating subconfluent ASZ001 and BSZ001 cells in 96-well plates in low-serum medium followed by addition of inhibitors or lentiviral shRNAs. MTS assays were carried out according to the manufacturer's instructions (Promega) 72 h after viral transduction or inhibitor treatment. Expression of protein and RNA was measured in stably transduced cells within three passages or at 24 h after inhibitor treatment. Transient knockdown for SRF, MKL, Phactr1, and KDM3A was achieved through transfecting ASZ001 cells with antisense siRNAs (Sigma-MISSION). Transfection using siRNAs was carried out with RNAiMAX transfection reagent (Thermo Fisher). qPCR was performed to measure expression of SRF and the hedgehog target GLI1.

The following inhibitors were used to suppress activity of the signaling proteins indicated below: MKL1 (CCG-1423, CCG-203971, CCG-100602; Cayman Chemical), Smoothened (vismodegib; Selleckchem), MEK1 and MEK2 (PH797804 and UO126; Selleckchem), p38 MAP kinase (SB239063; Tocris Bioscience), RHO (RHO inhibitor I; Cytoskeleton Inc.), ROCK (thiazovivin and Y-27632; Selleckchem), and mDia (SMIFH2; Sigma). Small molecules were used to stimulate activity of adenylyl cyclase (forskolin; Selleckchem) and Smoothened (SAG; Cayman Chemical).

Patient tumor explant culture and drug treatment. Freshly resected tumors were obtained from patients with advanced BCC receiving Mohs surgery. Informed consent was obtained in writing for all patient samples and was reviewed by the Stanford University Institutional Review Board. The tumor subtype was verified through immediate histological examination of resected BCCs. Patient specimens were cultured in EpiLife medium supplemented with 0.05 mM CaCl$_2$. Pharmacological inhibitors (CCG-1423 and vismodegib) were incubated with tumor specimens for 24 h. Drug-treated tissues were suspended in RLT buffer (Qiagen) and homogenized using 2 ml tissue lysing matrix E tubes (MP Biomedicals). RNA was isolated from tumors using the RNeasy standard protocol (Qiagen). RNA extracts were used to carry out qPCR with TaqMan probes for human GLI1 and GAPDH (Thermo Fisher). MKL1 localization was assessed in explant specimens through freezing samples in O.C.T. reagents and sectioning blocks for immunofluorescence analysis.

Statistical analysis. Experimental data for *in vitro* assays were tested for statistical significance against the respective controls using an unpaired Student's *t*-test. All *in vitro* assays were carried out in triplicate ($n = 3$) unless otherwise noted. For initial mouse RNA and exome sequencing, $n = 4$ for each group (sensitive and resistant). Statistically significant changes in expression for resistant versus sensitive tumors were determined using the DEseq algorithm with a cutoff of $P < 0.05$. GSEA data were analyzed using an FDR cutoff of 0.2 and $P < 0.05$. IF staining profiles (**Fig. 4c,d,f,g** and **Supplementary Fig. 11**) were analyzed for similarity compared to a cytoplasmic marker (KRT14) using Pearson's correlation analysis. For IF analyses, $n = 16$ for resistant and $n = 14$ for sensitive mouse tumors, and $n = 24$ for resistant and $n = 11$ for sensitive human tumors. For *in vivo* inhibitor studies in mice (**Fig. 6a,b**), biological replicates comprising four distinct tumors per condition were used to provide n ($n = 4$). For human patient explant inhibitor studies (**Fig. 6g–k**), ten tumors were analyzed using four experimental technical replicates ($n = 4$) per data point shown in **Figure 6h,j,k** and **Supplementary Figure 18**. No mouse or human tumors were excluded from our studies. Statistical significance for P values obtained in all figures is indicated. A normal distribution was observed for all data.

Life sciences reporting summary. Further information on experimental design and reagents is available in the **Life Sciences Reporting Summary**.

Data availability. Mouse RNA-seq and exome sequencing data generated in this manuscript are available using GEO identifier GSE78497.Human whole-exome sequencing and RNA-seq data sets from previous studies are publically available and can be found using GEO accession codes GSE58374, GSE58375, GSE58376, and GSE58377.

45. Wang, G.Y., Wang, J., Mancianti, M.L. & Epstein, E.H. Jr. Basal cell carcinomas arise from hair follicle stem cells in *Ptch1*^{+/−} mice. *Cancer Cell* **19**, 114–124 (2011).

46. Kuleshov, M.V. *et al.* Enrichr: a comprehensive gene set enrichment analysis web server 2016 update. *Nucleic Acids Res.* **44**, W90–W97 (2016).

47. Peterson, K.A. *et al.* Neural-specific Sox2 input and differential Gli-binding affinity provide context and positional information in Shh-directed neural patterning. *Genes Dev.* **26**, 2802–2816 (2012).

48. Lee, E.Y. *et al.* Hedgehog pathway–regulated gene networks in cerebellum development and tumorigenesis. *Proc. Natl. Acad. Sci. USA* **107**, 9736–9741 (2010).

49. Vokes, S.A., Ji, H., Wong, W.H. & McMahon, A.P. A genome-scale analysis of the *cis*-regulatory circuitry underlying sonic hedgehog–mediated patterning of the mammalian limb. *Genes Dev.* **22**, 2651–2663 (2008).

50. Sullivan, A.L. *et al.* Serum response factor utilizes distinct promoter- and enhancer-based mechanisms to regulate cytoskeletal gene expression in macrophages. *Mol. Cell. Biol.* **31**, 861–875 (2011).

51. McLean, C.Y. *et al.* GREAT improves functional interpretation of *cis*-regulatory regions. *Nat. Biotechnol.* **28**, 495–501 (2010).

52. Noubissi, F.K. *et al.* Role of CRD-BP in the growth of human basal cell carcinoma cells. *J. Invest. Dermatol.* **134**, 1718–1724 (2014).

nature research

Corresponding author(s): Anthony E. Oro

☐ Initial submission   ☐ Revised version   ☒ Final submission

Life Sciences Reporting Summary

Nature Research wishes to improve the reproducibility of the work that we publish. This form is intended for publication with all accepted life science papers and provides structure for consistency and transparency in reporting. Every life science submission will use this form; some list items might not apply to an individual manuscript, but all fields must be completed for clarity.

For further information on the points included in this form, see Reporting Life Sciences Research. For further information on Nature Research policies, including our data availability policy, see Authors & Referees and the Editorial Policy Checklist.

▶ Experimental design

1. Sample size

Describe how sample size was determined.

All available tumor tissue was used for sequencing and subsequent informatics/statistical analysis, and staining quantification. (Reported in Results pg 11 par 1, Methods pg 19 par 2, and Figure Legends pg 31 par 1, pg 33 par 2, and pg 34 par 2, Extended Data Fig. 1a)

In order to uncover all potential resistance mechanisms, initial tumor screening was carried out using sequencing of all available mouse tumor tissue (Fig. 1 and Extended Data Fig. 1a). Our follow up (efficacy) study was carried out using all tumors available which were matched by lineage for control and treatment groups (Fig. 6).

2. Data exclusions

Describe any data exclusions.

No data exclusions were needed.

3. Replication

Describe whether the experimental findings were reliably reproduced.

All in vitro experiments were reproduced a minimum of three times. In vivo drug delivery experiments were repeated in two independent parental tumor lines (Fig. 6 and Supp Fig. 5).

4. Randomization

Describe how samples/organisms/participants were allocated into experimental groups.

No randomization was necessary for our animal studies due to controlling for tumor lineage. No randomization was necessary for human clinical samples because all samples were used to describe pathway activation status and drug response.

5. Blinding

Describe whether the investigators were blinded to group allocation during data collection and/or analysis.

No blinding was necessary.

Note: all studies involving animals and/or human research participants must disclose whether blinding and randomization were used.

6. Statistical parameters

For all figures and tables that use statistical methods, confirm that the following items are present in relevant figure legends (or in the Methods section if additional space is needed).

n/a	Confirmed
☐	☒ The <u>exact sample size</u> (*n*) for each experimental group/condition, given as a discrete number and unit of measurement (animals, litters, cultures, etc.)
☐	☒ A description of how samples were collected, noting whether measurements were taken from distinct samples or whether the same sample was measured repeatedly
☐	☒ A statement indicating how many times each experiment was replicated
☐	☒ The statistical test(s) used and whether they are one- or two-sided (note: only common tests should be described solely by name; more complex techniques should be described in the Methods section)
☐	☒ A description of any assumptions or corrections, such as an adjustment for multiple comparisons
☐	☒ The test results (e.g. *P* values) given as exact values whenever possible and with confidence intervals noted
☐	☒ A clear description of statistics including <u>central tendency</u> (e.g. median, mean) and <u>variation</u> (e.g. standard deviation, interquartile range)
☐	☒ Clearly defined error bars

See the web collection on statistics for biologists for further resources and guidance.

▶ Software

Policy information about availability of computer code

7. Software

Describe the software used to analyze the data in this study.

> All analyses were carried out using GraphPad Prism v 7.0 and Microsoft Excel.

For manuscripts utilizing custom algorithms or software that are central to the paper but not yet described in the published literature, software must be made available to editors and reviewers upon request. We strongly encourage code deposition in a community repository (e.g. GitHub). *Nature Methods* guidance for providing algorithms and software for publication provides further information on this topic.

▶ Materials and reagents

Policy information about availability of materials

8. Materials availability

Indicate whether there are restrictions on availability of unique materials or if these materials are only available for distribution by a for-profit company.

> There are no restrictions on unique materials used in our manuscript. We have preserved additional tumor sample from mouse and human tumors which are available for future studies.

9. Antibodies

Describe the antibodies used and how they were validated for use in the system under study (i.e. assay and species).

Antibodies and dilutions for use in immunofluorescence experiments are reported in Methods (pg 21 par 3 and pg 23 par 2): Rabbit anti-SRF (1:100, Santa Cruz Biotechnology, sc-335, citation: Franco, C.A. et al. 2013. SRF selectively controls tip cell invasive behavior in angiogenesis. Development (Cambridge, England). 140: 2321-33.), chicken anti-keratin 14 (1:500, Abcam, ab130102, citation: Yang Z1, Hai B, Qin L, Ti X, Shangguan L, Zhao Y, Wiggins L, Liu Y, Feng JQ, Chang JY, Wang F, Liu F. Cessation of epithelial Bmp signaling switches the differentiation of crown epithelia to the root lineage in a β-catenin-dependent manner. Mol Cell Biol. 2013 Dec;33(23):4732-44. doi: 10.1128/MCB.00456-13. Epub 2013 Sep 30.), Gli1 (1:100, R&D Systems, AF3455, citation: Cigna N, Farrokhi Moshai E, Brayer S, Marchal-Somme J, Wemeau-Stervinou L, Fabre A, Mal H, Leseche G, Dehoux M, Soler P, Crestani B, Mailleux A. The hedgehog system machinery controls transforming growth factor-beta-dependent myofibroblastic differentiation in humans: involvement in idiopathic pulmonary fibrosis. Am J Pathol, 2012;181(6):2126-37. and, Strand MF, Wilson SR, Dembinski JL, Holsworth DD, Khvat A, Okun I, Petersen D, Krauss S. A novel synthetic smoothened antagonist transiently inhibits pancreatic adenocarcinoma xenografts in a mouse model. PLoS ONE, 2011;6(6):e19904.), MRTF-A (1:200, Sigma, HPA030782. citation: Record J, Malinova D, Zenner HL, Plagnol V, Nowak K, Syed F, Bouma G, Curtis J, Gilmour K, Cale C, Hackett S, Charras G, Moulding D, Nejentsev S, Thrasher AJ, Burns SO. Immunodeficiency and severe susceptibility to bacterial infection associated with a loss-of-function homozygous mutation of MKL1. Blood , 2015 Sep 24; 126(13):1527-35.), beta tubulin (1:500, DSHB, E7 citation: Jain S1, Welshhans K1,2. Netrin-1 induces local translation of down syndrome cell adhesion molecule in axonal growth cones. Dev Neurobiol. 2015 Oct 31.).

Additional antibody controls were carried out by our group for SRF (Supp Fig. 7), Gli1 (Supp Fig 10 and Supp Fig. 15), Rho-GTP (Supp Fig. 16), and MRTF-A (Supp Fig. 18).

10. Eukaryotic cell lines

a. State the source of each eukaryotic cell line used.

ASZ and BSC were generated from mouse BCCs (ref: So PL1, Langston AW, Daniallinia N, Hebert JL, Fujimoto MA, Khaimskiy Y, Aszterbaum M, Epstein EH Jr. Long-term establishment, characterization and manipulation of cell lines from mouse basal cell carcinoma tumors. Exp Dermatol. 2006 Sep;15(9):742-50). NIH 3T3 cells were obtained from ATCC.

b. Describe the method of cell line authentication used.

BCC cell lines were verified using Ptch1- reporter beta-gal staining which marks tumors cells generated in the mouse referenced above. NIH-3T3 cells were certified by ATCC.

c. Report whether the cell lines were tested for mycoplasma contamination.

Our cell lines are regularly tested for mycoplasma using the MycoAlert detection kit (Lonza LT07-418).

d. If any of the cell lines used are listed in the database of commonly misidentified cell lines maintained by ICLAC, provide a scientific rationale for their use.

None of the cell lines used are listed in the database of commonly misidentified cell lines.

▶ Animals and human research participants

Policy information about studies involving animals; when reporting animal research, follow the ARRIVE guidelines

11. Description of research animals

Provide details on animals and/or animal-derived materials used in the study.

Experimental Ptch1+/− K14-Cre-ER2 p53fl/fl (BCC) mice were comprised of females generated in the C57BL6 background. Mice were 9-weeks old at the time of irradiation. Recipient NOD-SCID mice were 9-weeks old at the time of tumor passage and initiation of drug treatment.

Policy information about studies involving human research participants

12. Description of human research participants

Describe the covariate-relevant population characteristics of the human research participants.

All human samples were deidentified and our group was blinded to all characteristics of human subjects except in cases were patients contained sensitive or resistant tumors. Human data was obtained after Stanford Human Subjects panel approval, and written informed consent was obtained for all subjects.